**Infinite Science
Publishing**

Research Article

Improved Image Reconstruction in Magnetic Particle Imaging using Structural a priori Information

Christine Bathke[a,*] · Tobias Kluth[a] · Christina Brandt[b] · Peter Maass[a]

[a]Center for Industrial Mathematics, University of Bremen, Bremen, Germany
[b]Department of Applied Physics, University of Eastern Finland, Kuopio, Finland
*Corresponding author, email: cbathke@math.uni-bremen.de

Abstract

Magnetic particle imaging is a tracer-based imaging modality developed to detect the concentration of superparamagnetic iron oxide nanoparticles. The capability for imaging is due to the high sensitivity to the nanoparticle's nonlinear response to the applied magnetic field. This modality relies on the spatial distribution of the tracer material which makes it suitable for applications such as imaging blood flow or tracking medical instruments without the need of harmful radiation. Magnetic particle imaging benefits from a high temporal resolution, but it also suffers from missing background information, e.g., from biological tissue. Commonly the lack of information is remedied by magnetic resonance imaging. Image reconstructions from both modalities are computed independently and aligned subsequently to allow inferences. We use the additional information commonly provided by magnetic resonance imaging to improve the reconstruction in magnetic particle imaging. For this purpose, a Tikhonov-type functional is equipped with a structural prior where the additional information is incorporated. By minimizing this functional, we obtain improved reconstructions of the concentration of nanoparticles which is illustrated in numerical simulations.

I. Introduction

Magnetic particle imaging (MPI) is a tracer-based imaging modality developed to detect the concentration of superparamagnetic iron oxide nanoparticles [1]. It is highly sensitive to the nanoparticle's nonlinear response to the applied magnetic field and allows a fast data acquisition [2]. The high temporal resolution makes MPI suitable for applications such as imaging blood flow or tracking medical instruments [3–5]. The concentration of nanoparticles, which contains not necessarily any further anatomical information, is determined by the fast change of the applied magnetic field. The magnetic field is designed in a way such that a field free point (FFP), respectively a field free line, is moved along a certain trajectory. The dynamic of the magnetic field causes a measurable change of the nanoparticle's magnetization.

The present paper deals with rapid MPI sequences generated by moving the FFP along Lissajous curves. Since the system matrix therefore obeys a complex structure, the matrix, which is challenging to model, is usually measured [6, 7] although there are some approaches for a model-based reconstruction [8, 9]. In the case of Cartesian sequences as used in [10–12], the MPI signal can be described by a simple coordinate trans-

formation followed by a spatial convolution. These reconstruction methods [13, 14] known as X-space reconstruction for these types of sequences are usually not formulated as an inverse problem.

Since the considered reconstruction in MPI is an ill-posed inverse problem [9, 15], it requires regularization. Current reconstruction methods are based on Tikhonov-type regularization [3, 16–18]. Direct solvers such as QR decomposition or singular value decomposition are in practice computationally too expensive for large system matrices such that the corresponding normal equation is solved iteratively. Most of the published papers considering Lissajous type MPI sequences apply the regularized Kaczmarz method, known also as algebraic reconstruction technique [3, 16, 19, 20]. The Kaczmarz method shows fast convergence due to the fact that the rows of the system matrix are close to orthogonal. Moreover, a nonnegativity constraint [3] for the particle concentration can be included easily. In some publications [16], a diagonal weighting matrix is introduced in the Tikhonov-regularization which weights the individual rows of the system matrix and the measurement vector.

In MPI the tracer concentration is reconstructed which does not contain any other anatomical information. As a result, MPI is often conducted together with magnetic resonance imaging (MRI). It is common practice that MPI and MRI measurements are performed in different scanners [3, 19] requiring a subsequent alignment of both reconstructions. For example, this is done by hand in [5], where the authors show how to track a labeled angioplasty-catheter in-vitro when removing a stenosis. Existing bimodal MPI-MRI scanners [21, 22] allow to perform both measurements without moving the subject which simplifies image registration and allows to improve the MPI reconstruction using information from another modality.

Bimodal reconstruction techniques can follow two different approaches. On the one hand, a joint reconstruction problem coupling both inversions is solved. On the other hand, the reconstruction from one modality is used as a priori information for the second modality. We follow the latter approach to incorporate MRI information into the MPI reconstruction. However, this problem is already addressed in other applications. For example, MRI is used in combination with positron emission tomography [23, 24]. Structural information from computer tomography is also used for this purpose. Multi-contrast images, which can be seen as another information source, are used in MRI [25].

Methods can be distinguished by the kind of image information used in the reconstruction process. Information theoretical measures can improve reconstructions [26]. Another possibility is the extraction of structural information, i.e. of features such as edges, from the image and the incorporation into the recon-

struction [27, 28]. However, none of these methods have been already applied to the MPI problem with a priori information given by MRI.

Therefore, we will assume in the following that we have a MRI image as a priori information available. We will propose a new image reconstruction method for MPI based on a Tikhonov-regularization with total variation as penalty term. Our goals are the following: (1) a definition of a regularization method which improves the reconstruction compared to the start-of-the-art methods; (2) a derivation of a solver adapted to the needs of MPI; (3) a demonstration of the advantages of our proposed method with help of numerical tests.

In order to achieve the first goal, we propose to use a weighted total variation as regularizing term where structural information from an a priori image is incorporated. This term will promote sparsity in the gradient of the image and will favor edges which are also present in the a priori image. Moreover, in order to obtain positive particle concentrations, we add a non-negativity constraint. As an efficient solver for the minimization problem, we adapt an algorithm proposed in [25] to the specific needs of MPI. It is a splitting method based on the alternating method of multipliers. For the last goal, we conduct a series of simulated experiments with known ground truth. The results show that the proposed method improves the image quality significantly compared to pure total variation regularization and even more to the state-of-the art reconstruction with respect to visual inspection as well as to image quality measures.

This paper is organized as follows. In Sec. II, the MPI reconstruction problem is first formulated, and the proposed method is motivated. Moreover, a weighted total variation is defined which incorporates the a priori edge information into the proposed variational regularization method. The resulting minimization problem of the Tikhonov-functional is solved by a splitting method, which is derived in Sec. III. In Sec. IV, we conduct a simulation study and demonstrate that the proposed method with edge information from the a priori image significantly improves the image quality.

II. Methods

II.I. Problem formulation

Magnetic particle imaging does not provide information about the background, for example from tissue. As a result, several studies, which primarily address magnetic particle imaging, use MRI images as a reference [3, 5, 19]. For example in [3], a MRI image of a mouse is used to allow reasoning from the MPI reconstruction. For this purpose, the MRI image is aligned to the vena cava and the heart chambers. The

main criteria to do the alignment by hand are common features of landmarks. We can find edges, e.g. the vascular walls of the vena cava, which both the MPI and MRI image have in common. These studies have all in common that the MPI problem is solved independently of the available a priori information given by a previously computed MRI image.

The problem of reconstructing the concentration from the MPI signal is formulated as a discrete linear inverse problem motivated by the measured system matrix [7]. Let the concentration function $c : \Omega \to \mathbb{R}_+$, $d = 2, 3$, $\Omega \subset \mathbb{R}^d$ bounded, be an element of a function space X. We assume a given basis $\{\phi_i\}_{i=1,\dots,N} \subset X$, $N \in \mathbb{N}$, of a finite-dimensional subspace $X_N \subset X$. From the application point of view, piecewise constant functions are a reasonable assumption for these basis functions as they may represent a "delta"-probe which is moved over the entire region Ω [7]. In MPI time-dependent magnetic fields are applied, and time-dependent potentials are measured. However, due to the analog filter process in the signal acquisition chain, the MPI reconstruction problem is commonly formulated in frequency space by computing the discrete Fourier transform of the measured time signal. Inserting a finite-dimensional concentration $\tilde{c} = \sum_{i=1}^{N} c_i \phi_i \in X_N$ in the MPI reconstruction problem results in the system of linear equations given by

$$u_k = \int_\Omega \tilde{c}(x) s_k(x) \, dx = \sum_{i=1}^{N} c_i \underbrace{\int_\Omega s_k(x) \phi_i(x) \, dx}_{=: s_{ki}} \quad (1)$$

for $k = 1, \dots, K$, $K \in \mathbb{N}$ where $u_k \in \mathbb{C}$ is the Fourier coefficient of the k-th frequency and $s_k : \Omega \to \mathbb{C}$ is the respective Fourier coefficient function being an element of a function space Y. To guarantee the existence of the matrix entries s_{ki}, a standard choice of function spaces is $X = Y = L^2(\Omega)$. The problem of reconstructing the concentration function thus reduces to the discrete linear inverse problem given by

$$Sc = u, \quad (2)$$

where $c \in \mathbb{R}_+^N$ is the tracer concentration, $S \in \mathbb{C}^{K \times N}$ is the system matrix in frequency space and $u \in \mathbb{C}^K$ contains the measured Fourier coefficients. The prior information is an already reconstructed MRI image and is denoted by $v \in \mathbb{R}_+^N$.

II.II. Structural a priori information

The solution of the MPI problem in Eq. (2) is determined by minimizing a Tikhonov functional

$$J_\alpha(c) = \frac{1}{2}\|Sc - u\|^2 + \alpha \mathscr{R}(c), \quad (3)$$

where the a priori information provided by the MRI image is considered in the regularization term $\mathscr{R}$. Here and in the remainder of this article $\| \cdot \|$ denotes the Euclidean norm. By minimizing the functional J_α, the discrepancy term forces the solution to fit the data. Simultaneously the regularization term enforces the solution to fulfill the assumed properties. The impact of the regularization is controlled by the regularization parameter α. The standard case $\mathscr{R}(c) = 1/2\|c\|^2$ is commonly used to compute MPI reconstructions [16]. More sophisticated regularization techniques including sparseness and total variation assumptions were recently applied to MPI [29]. In order to improve the MPI reconstruction, we use an adapted weighted total variation penalty term which is motivated by the structure both MRI and MPI images have in common.

First, we introduce the standard total variation (TV) penalty term [30]. The discrete TV term is given by the l_1-norm of the gradient of the image c, i.e., $\mathrm{TV} : \mathbb{R}^N \to \mathbb{R}_+$ with

$$\mathrm{TV}(c) = \sum_{n=1}^{N} \|\nabla c_n\|, \quad (4)$$

where $\nabla c_n \in \mathbb{R}^d$, $n = 1, \dots, N$, is the discretized gradient with respect to the location. This functional is convex, favors denoising and preserves edges, but it does not take additional information into account.

A natural extension of this approach is the introduction of spatially dependent weights $w_n \in [0, 1]$, $n = 1, \dots, N$, (see also [31] for the continuous case) resulting in a functional $\mathrm{wTV} : \mathbb{R}^N \to \mathbb{R}_+$,

$$\mathrm{wTV}(c) = \sum_{n=1}^{N} w_n \|\nabla c_n\|. \quad (5)$$

The weights can be determined by the a priori image information given from another modality. Gradient information of the MRI image v might be used as an indicator for regions containing an edge. A small weight w_n is assigned to a large gradient in the MRI image, i.e $\|\nabla v_n\|$ is large, to favor edges in this particular region in the concentration function. Regions having a small gradient in the MRI image get a larger weight. There are several ways to implement the behavior of the weights in dependence of the MRI image v. It could be determined by contrast [32] or orientation [33] only which is disadvantageous if the scaling of the a priori image differs from the reconstructed image. The latter case is named directional total variation by the authors of [33]. But in our setup, no favored orientation exists such that a weighting depending solely on the orientations in the MRI image is not reasonable. One feature which was used primarily in the alignment process is the relation between the orientations of the gradient in the MRI image and

the reconstructed concentration. If both gradients are parallel, an edge is more reasonable in this region which is realized by a small weight. And if the gradients are orthogonal, the weight should be large. This behavior cannot be realized by a weighting depending solely on the a priori information. Therefore, the weights are assumed to be functions $w_n : \mathbb{R}^N \to [0,1]$, $n = 1, \ldots, N$, with $w_n(c) = g_n(c, v)$ for a given $v \in \mathbb{R}^N$ and a function $g : \mathbb{R}^N \times \mathbb{R}^N \to [0,1]^N$ describing the relation between both reconstructions. The penalty term thus becomes

$$\mathscr{R}(c) = \sum_{n=1}^{N} w_n(c) \|\nabla c_n\|. \qquad (6)$$

The desired behavior can be implemented by a variety of functions g. A particular intuitive choice can be formulated by the angle between both gradients. Let $\beta : \mathbb{R}^d \times \mathbb{R}^d \to [0, 2\pi)$ be the angle between the two input vectors. Then a reasonable weighting can be defined by $g_n(v, c) = |\sin(\beta(\nabla v_n, \nabla c_n))|$ if $v, c \in \mathbb{R}^N$ have nonzero gradients $\nabla v_n, \nabla c_n$. If one of the gradients is zero, $g_n(v, c) = 1$ holds. The smaller the angle between both gradients, the smaller is the influence of the penalty term, i.e., edges are less penalized in the particular region.

The formulation of the penalty term in terms of trigonometric functions gives an intuitive geometric interpretation. But for minimizing the functional J_α, we use the following equivalent formulation of $\mathscr{R}$, which can be related to existing algorithmic approaches. Using the following equality for $\nabla v_n, \nabla c_n \neq 0$

$$\begin{aligned}
w_n(c) &= |\sin(\beta(\nabla v_n, \nabla c_n))| \\
&= \left(1 - \frac{\langle \nabla v_n, \nabla c_n \rangle^2}{\|\nabla v_n\|^2 \|\nabla c_n\|^2}\right)^{1/2} \\
&= \frac{1}{\|\nabla c_n\|} \left(\langle \nabla c_n, \nabla c_n \rangle - \langle \frac{\nabla v_n}{\|\nabla v_n\|}, \nabla c_n \rangle^2 \right)^{1/2} \\
&= \frac{1}{\|\nabla c_n\|} \left\| \nabla c_n - \langle \frac{\nabla v_n}{\|\nabla v_n\|}, \nabla c_n \rangle \frac{\nabla v_n}{\|\nabla v_n\|} \right\| \\
&= \frac{1}{\|\nabla c_n\|} \left\| \left(I - \frac{\nabla v_n}{\|\nabla v_n\|} \frac{\nabla v_n^T}{\|\nabla v_n\|} \right) \nabla c_n \right\|,
\end{aligned}$$
$$(7)$$

we arrive at the following penalty term

$$\begin{aligned}
&w_n(c) \|c_n\| \\
&= \begin{cases} \left\| \left(I - \frac{\nabla v_n \nabla v_n^T}{\|\nabla v_n\|^2} \right) \nabla c_n \right\|, & \nabla v_n, \nabla c_n \neq 0 \\ \|\nabla c_n\|, & \text{else} \end{cases}
\end{aligned} \qquad (8)$$

defined for two different cases. To combine these cases, we need to avoid division by zero and introduce an $\epsilon > 0$. Then the penalty term in Eq. (6) becomes

$$\mathscr{R}(c) = \sum_{n=1}^{N} \left\| \left(I - \frac{\nabla v_n \nabla v_n^T}{\|\nabla v_n\|^2 + \epsilon} \right) \nabla c_n \right\|, \qquad (9)$$

which is equal to the term (8) in the second case of $\nabla v_n, \nabla c_n = 0$. For the first case $\nabla v_n, \nabla c_n \neq 0$, the equality holds in the limit $\epsilon \to 0$.

This penalty term is also named directional total variation by some other authors [25]. Note that the terminology is used inconsistently in the literature as other authors [33] use this term for a different kind of functional. To obtain a reconstruction of the concentration, we use the following algorithmic approach to minimize the functional J_α.

III. Algorithmic approach

For minimizing problem (3) with the penalty term given in Eq. (9), we mainly follow Ehrhardt and Betcke [25] and adapt the algorithm to MPI where necessary. Instead of solving this problem as a whole, we split it into two less complex subproblems. Introducing a second variable x in the penalty term and requiring both variables c and x to be equal leads to the equivalent minimization problem

$$\min_{c,x \in \mathbb{R}_+^N} \frac{1}{2} \|Sc - u\|^2 + \alpha \mathscr{R}(x) \text{ such that } c = x \quad (10)$$

with the associated scaled augmented Lagrangian

$$\mathscr{L}_\rho(c, x, \lambda) = \|Sc - u\|^2 + \alpha \mathscr{R}(x) + \frac{\rho}{2} \|c - x + \lambda\|^2 - \frac{\rho}{2} \|\lambda\|^2 \qquad (11)$$

with the Lagrange multiplier $\lambda \in \mathbb{C}^N$ and the penalty parameter $\rho > 0$. A common technique to solve this kind of problem is the alternating direction method of multipliers (ADMM) [34] consisting of the following three steps

$$c^{k+1} = \arg \min_{c \in \mathbb{C}^N} \frac{1}{2} \|Sc - u\|^2 + \frac{\rho}{2} \|c - x^k + \lambda^k\|^2 \qquad (12)$$

$$x^{k+1} = \arg \min_{x \in \mathbb{R}_+^N} \alpha \mathscr{R}(x) + \frac{\rho}{2} \|c^{k+1} - x + \lambda^k\|^2 \quad (13)$$

$$\lambda^{k+1} = \lambda^k + c^{k+1} - x^{k+1}. \qquad (14)$$

In every iteration the two subproblems are minimized in an alternating manner. In the first step, we allow the tracer concentration c to be complex valued and negative because this more general problem can be solved more efficiently. Since the solution of the minimization problem (13) in the next step does not depend on the imaginary part of c^{k+1}, this generalization does not affect the solution of the overall problem. In the following second step, we force the solution x to be nonnegative and real. Since the constraint $c = x$ requires both variables to be equal, the output of these first two steps is a physically reasonable tracer concentration which is nonnegative and real. Afterwards the Lagrangian multiplier is updated. We also vary

the penalty parameter ρ to improve convergence. For details on this as well as a stopping criterion, we refer to [34]. The ADMM for MPI reconstruction can be found in Alg. 1.

Let us now look at the minimization of the two subproblems. The optimality condition of the first problem (12) is

$$
\begin{aligned}
0 &= \nabla_c \left(\frac{1}{2}\|Sc - u\|^2 + \frac{\rho}{2}\|c - x^k + \lambda^k\|^2 \right) \\
&= \langle S, Sc - u \rangle + \rho\langle 1, c - x^k + \lambda^k \rangle \\
&= \langle 1, S^*Sc + \rho c \rangle - \langle 1, S^*u + \rho(x^k - \lambda^k) \rangle.
\end{aligned}
$$

Hence, we need to solve the linear equation system

$$
(S^*S + \rho I)c^{k+1} = (S^*u + \rho(x^k - \lambda^k)), \quad (15)
$$

which we solve numerically using the MATLAB implementation of the biconjugate gradients method (function bicg) [35].

Algorithm 1 ADMM for MPI reconstruction using prior information

Input:
  $u \in \mathbb{C}^K$ MPI data
  $\alpha > 0$ regularization parameter
  $S \in \mathbb{C}^{K \times N}$ system matrix
  $n_{\text{iter}} \in \mathbb{N}$ maximum number of iterations
Output:
  $x^k \in \mathbb{R}_+^N$ reconstructed tracer
 1: **function** ADMM_MPI$(u, \alpha, S, n_{\text{iter}})$
 2:     $\rho \leftarrow 1, x^0, \lambda^0 \leftarrow 0$ ▷ initialize variables
 3:     **for** $i = 0 : n_{\text{iter}}$ **do**
     update minimization problems
 4:         $c^{k+1} \leftarrow (S^*S + \rho I)^{-1}(S^*u + \rho(x^k - \lambda^k))$
 5:         $x^{k+1} \leftarrow \text{prox}_{\alpha/\rho \mathscr{R} + \chi_{[0,\infty)^N}}(c^{k+1} + \lambda^k)$ ▷
     apply Alg. (2)
     update Lagrange multipliers
 6:         $\lambda^{k+1} \leftarrow \lambda^k + c^{k+1} - x^{k+1}$
     update ρ and check for convergence   ▷ see [34]
 7:     **end for**
 8:     **return** x^k
 9: **end function**

The second problem, as seen in Eq. (13), can be written as proximal mapping

$$
\text{prox}_{\alpha\mathscr{R} + \chi_{[0,\infty)^N}}(y) := \arg\min_{x \in \mathbb{R}_+^N} \left\{ \frac{\|x - y\|^2}{2} + \alpha\mathscr{R}(x) \right\}, \quad (16)
$$

where $y := c^{k+1} + \lambda^k$. To keep notations short, we denote the weights given in Eq. (9) as

$$
D_n = I - \frac{\nabla v_n \nabla v_n^T}{\|\nabla v_n\|^2 + \epsilon}. \quad (17)
$$

Analogous to the classic total variation [36], the authors of [25] propose to dualize the structural total variation as

$$
\mathscr{R}(x) = \sum_{n=1}^{N} \|D_n \nabla x_n\| = \sup_{p \in \mathbb{U}} \langle -\text{div}\, D^*p, x \rangle. \quad (18)
$$

Hence, instead of minimizing the l_1-norm of the weighted gradient, we can minimize the supremum of the divergence of the weighted gradient over the unit ball in the gradient space $\mathbb{U} = \{x \in \mathbb{R}^{d \times N} \mid \|x_n\| \leq 1\}$. As we discretize the gradient as forward differences, the matching discrete divergence is approximated by backward differences. The multiplication D^*p denotes the multiplication of a matrix field $D^* \in \mathbb{R}^{d \times d \times N}$ and the vector field $p \in \mathbb{R}^{d \times N}$, i.e. the product of $D_n^* \in \mathbb{R}^{d \times d}$ and $p_n \in \mathbb{R}^d$ in every component n. Combining this dualization with Eq. (16) and applying the fast iterative shrinkage-thresholding algorithm (FISTA) [37] to compute the resulting proximal operator, they arrive at Alg. 2. This algorithm uses two different orthogonal projections, the projection onto the unit ball in gradient space

$$
P_{\mathbb{U}}(p_n) = \frac{1}{\max\{1, \|p_n\|\}} p_n \quad (19)
$$

and the projection $P_{[0,\infty)^N}$ onto the nonnegative real numbers.

Algorithm 2 Fast gradient projection method for structure-guided Total Variation

Input:
  $\alpha > 0$ regularization parameter
  $y \in \mathbb{C}^N$ proximal point
  $n_{\text{iter}} \in \mathbb{N}$ maximum number of iterations
  $D \in \mathbb{R}^{d \times d \times N}$ anisotropy (prior information)
  $s > 0$ step size for FISTA
Output:
  $x^k \in \mathbb{R}_+^N$ approximation of minimizer
 1: **function** projection_TV$(\alpha, y, n_{\text{iter}}, D, p^0, s)$
 2:     $t^0 \leftarrow 1, q^0, p^0 \leftarrow 0$ ▷ initialize variables
 3:     **for** $i = 1 : n_{\text{iter}}$ **do**
 4:         $g^k \leftarrow \alpha D \nabla P_{[0,\infty)^N}(y + \alpha\,\text{div}\, D^*q^{k-1})$ ▷
     compute gradient
 5:         $p^k \leftarrow P_{\mathbb{U}}(q^{k-1} + sg^k)$ ▷ update dual
     variable
 6:         $t^k \leftarrow \frac{1}{2}\left(1 + \sqrt{(1 + 4(t^{k-1})^2)}\right)$
 7:         $q^k \leftarrow p^k + \frac{t^{k-1}-1}{t^k}(p^k - p^{k-1})$
 8:     **end for**
 9:     $x^k \leftarrow P_{[0,\infty)^N}(y + \alpha\,\text{div}\, D^*p^k)$
10:     **return** x^k
11: **end function**

IV. Results

IV.I. Simulation setup

For the numerical tests, we built up a simulation framework for a 2D FFP scanner. Assuming isotropic particles with diameter 30 nm, we used the Langevin model of paramagnetism for modeling the magnetization. The measurements are simulated with a drive field amplitude 18 mT/μ_0 in both excitation directions and a gradient strength of $G_x = G_y = 2.75$ T/m/μ_0 and accordingly $G_z = 5.5$ T/m/μ_0. The Lissajous measurement circle with a repetition time of $T_R = 1$ ms is generated by a base frequency of 600 kHz and frequency dividers 24 and 25. The FOV is sampled at $44 \times 44 = 1936$ positions which leads to a size of 14.1×14.1 mm^2. Note that the area covered by the FFP trajectory is only slightly smaller, i.e. about 13.1×13.1 mm^2. In order to avoid inverse crime, we used a 3 times finer grid for the forward simulations. The phantoms used were scaled down to the coarser grid using bicubic interpolation. We added noise on the signal by using the noise model proposed in [38]. Frequencies higher than 45 kHz and up to 3 MHz have been stored leading to 5992 rows in the system matrix.
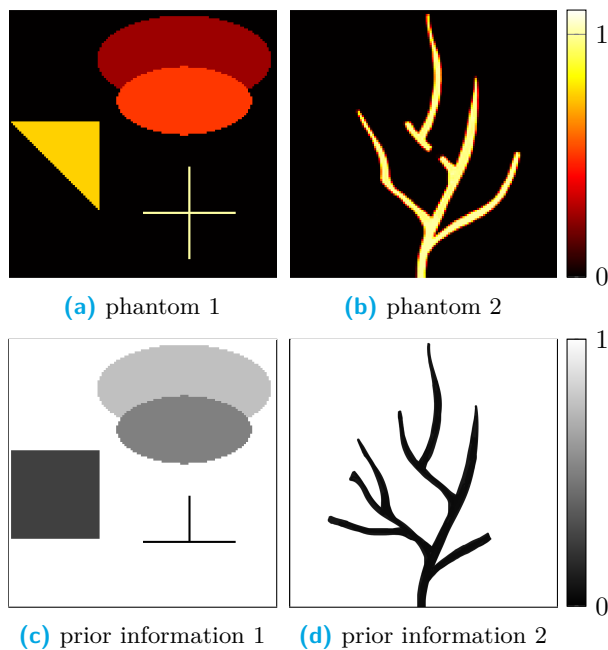

(a) phantom 1   **(b)** phantom 2

(c) prior information 1   **(d)** prior information 2

Figure 1: MPI phantoms (top row) and additional prior information (lower row).

We conducted our experiments using the two phantoms depicted in Fig. 1. The upper row shows the MPI phantoms used to simulate the data, while the lower row contains the additional prior information used for the reconstruction. Phantom 1 is an abstract composition of different sized areas with straight and round edges with different orientations taken from the examples of the MATLAB toolbox [39]. As all these features can be expected in a medical application, this phantom is used for a proof of principle. The second phantom resembles a vascular tree and illustrates how our algorithm would work on real data. For both our phantoms the prior information and the MPI phantom differ to show how our algorithm handles missing or superfluous data. We also included a stenosis in the MPI phantom of the vascular tree (in the middle) in order to compare different algorithms in handling small gaps.

IV.II. Reconstructions

Using the two different phantoms discussed in the previous subsection, we tested the proposed weighted total variation approach against classic total variation and a nonnegative Tikhonov regularization as state-of-the-art. The total variation reconstruction was realized using our ADMM algorithm without prior information (i.e. $v = 0$), whereas the nonnegative Tikhonov regularization was computed with a Kaczmarz implementation from the Github project page of [40]. We compared the outputs of the different algorithms for two different noise levels. In the low noise case we added 5 % Gaussian noise on the simulated MPI data and assumed the MRI image to be perfectly reconstructed. In the high noise case of 15 % on the MPI data, we also added 1 % Gaussian noise on the a priori informations. The penalty parameter α, balancing the influence of the used penalty term, was chosen empirically through visual inspection. Apart from assessing the reconstruction quality visually, we computed quantitative measures, i.e., peak-signal-to-noise ratio (PSNR) and structural similarity index (SSIM), where higher values indicate a higher reconstruction quality, and the Euclidian distance between the true solution $c^\dagger$ and the reconstructed image c.

The results for phantom 1 shown in Fig. 2 were generated using the parameters in Tab. 1, which also contains the PSNR and SSIM values for the reconstructed images. Looking at the tracer reconstructions in Fig. 2, one can observe that even at a lower noise level of 5 % the state-of-the-art algorithm, i.e. nonnegative Tikhonov regularization, is unable to reconstruct the cross at the bottom and the two ellipses at the top properly. The same is true for classic total variation which produces nevertheless a more homogenous image. In contrast, the weighted total variation provides sharp edges and homogenous areas due to the good a priori information. This is especially noticeable at the border of the images where the other algorithms fail because of the low sensitivity of the system matrix at the border of the field of view. This qualitative assessment is supported by the PSNR and SSIM values as well as

the Euclidean distance between the true solution and the reconstructed tracer concentration, which clearly indicate that the proposed approach gives the best reconstruction.
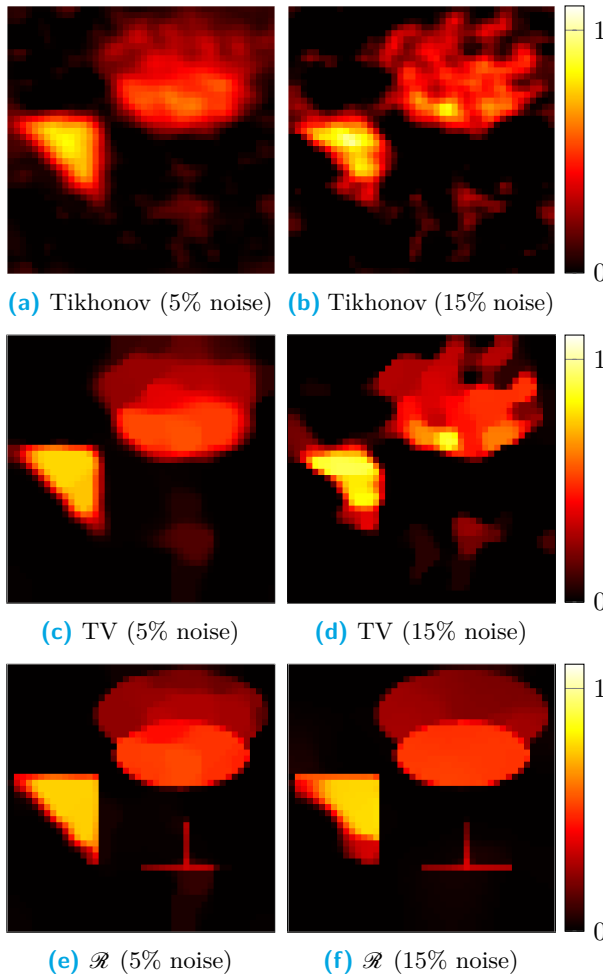

(a) Tikhonov (5% noise)   **(b)** Tikhonov (15% noise)

(c) TV (5% noise)   **(d)** TV (15% noise)

(e) $\mathscr{R}$ (5% noise)   **(f)** $\mathscr{R}$ (15% noise)

Figure 2: Comparison between nonnegative Tikhonov regularization (top row), TV regularization (middle row) and the proposed method (bottom row) for reconstructions of phantom 1 from noisy data corrupted with 5% (left column) and 15% (right column) Gaussian noise. The results computed with the proposed method show sharp edges and a high spatial homogeneity compared to the other two methods.

Fig. 3 depicts the reconstruction results of phantom 2, which were generated using the parameters in Tab. 2. Again this table also shows the quantitative measures. For this phantom, the nonnegative Tikhonov reconstructions look blurry with a noisy background, but remarkably the small gap that resembles a stenosis is visible. The images computed using the classic total variation have sharper edges, but for the high noise case the phantom is slightly distorted at the top branches, which is also observable for the Tikhonov regularization. Again the proposed approach offers visually the

Table 1: Regularization parameters used for reconstruction of phantom 1 (Fig. 2) and image quality measures.

Method	α	PSNR	SSIM	$\|c^\dagger - c\|$
		5% noise		
Tikhonov	$3 \cdot 10^{-1}$	18,1	0,673	5,46
TV	$1 \cdot 10^{-7}$	23,6	0,740	2,90
$\mathscr{R}$	$9 \cdot 10^{-8}$	27,4	0,874	1,88
		15% noise		
Tikhonov	$1 \cdot 10^{0}$	19,9	0,496	4,45
TV	$1 \cdot 10^{-7}$	19,7	0,605	4,54
$\mathscr{R}$	$1 \cdot 10^{-6}$	25,5	0,858	2,34

best reconstruction results. The branches in the reconstruction are the closest to their original form, and there is only little noise left in the background. One aspect which is reconstructed slightly better by classic total variation is the region where prior information is missing, i.e., the small gap in the middle branch and the missing tip at the right branch. Overall the differences in the outputs of the three methods are not as big as for the first phantom but still significant. This observation is reflected by the quantitative measurements found in Tab. 2.

Remarkably, the small gap in the middle branch is reconstructed better in the high noise case by the two total variation approaches. This is probably due to the bigger regularization parameters α which, in order to suppress the noise, puts more importance on the penalty terms compared to the low noise case. Since total variation favors piecewise homogenous reconstructions, edges appear sharper. One has to keep in mind that the regularization parameters have been chosen through visual inspection. For a more objective comparison of the different algorithms one could do a line search to find the optimal regularization parameter α regarding one of the quality measures listed in Tab. 2. Most likely the optimal parameters differ for each of these three quality measures.

Table 2: Regularization parameters used for reconstruction of vascular tree (Fig. 3) and image quality measures.

Method	α	PSNR	SSIM	$\|c^\dagger - c\|$
		5% noise		
Tikhonov	$3 \cdot 10^{-1}$	17,8	0,468	5,67
TV	$1 \cdot 10^{-9}$	19,4	0,841	4,73
$\mathscr{R}$	$2 \cdot 10^{-8}$	21,0	0,896	3,93
		15% noise		
Tikhonov	$5 \cdot 10^{-1}$	16,7	0,429	6,40
TV	$1 \cdot 10^{-8}$	17,0	0,640	6,24
$\mathscr{R}$	$7 \cdot 10^{-8}$	19,6	0,759	4,60

(a) Tikhonov (5% noise) **(b)** Tikhonov (15% noise)

(c) TV (5% noise) **(d)** TV (15% noise)

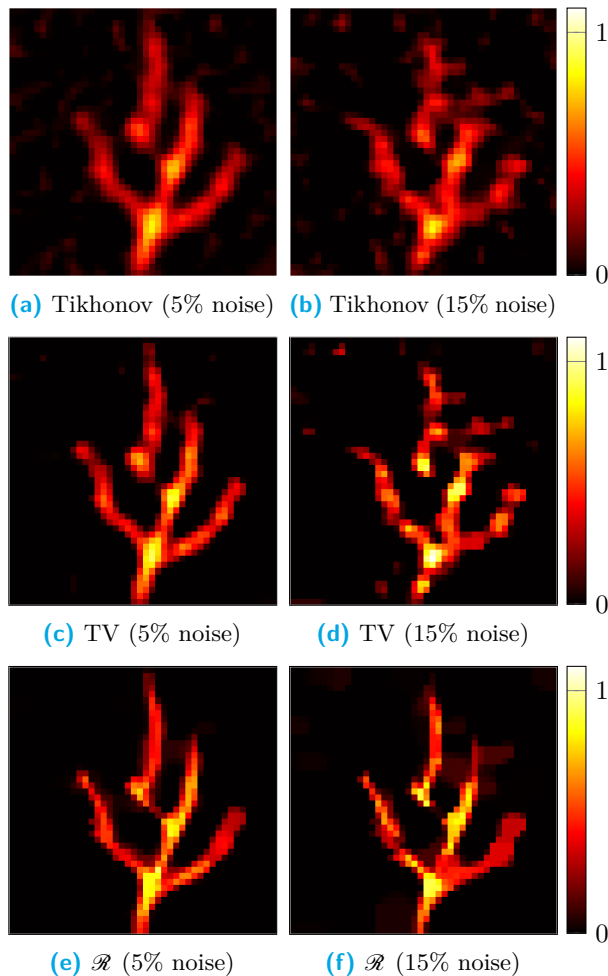**(e)** $\mathscr{R}$ (5% noise) **(f)** $\mathscr{R}$ (15% noise)

Figure 3: Comparison between nonnegative Tikhonov regularization (top row), TV regularization (middle row) and the proposed regularization (bottom row) for reconstructions of phantom 2 (vascular tree) from noisy data corrupted with 5 % (left column) and 15 % (right column) Gaussian noise. The proposed method shows clearly superior results, in particular for the high noise scenario.

V. Discussion

In the present simulation study, we show the potential to improve the MPI reconstructions by using structural a priori information. The improved reconstructions outperform the reconstructions determined by the commonly used nonnegative Tikhonov regularization and those computed by classic total variation qualitatively as well as quantitatively. They are particularly improved at edges which both the MPI reconstruction and the a priori image have in common. Although the a priori information favors equally oriented edges in the reconstruction, the phantoms are reconstructed correctly even if an edge is present in the a priori image but missing in the phantom. Several studies include MRI images to allow semantic inferences, and the num-

ber of hybrid scanners increases [3, 5, 19, 22]. This offers an ample opportunity to improve MPI reconstruction by applying new methodologies which exploit the additional information.

Possible applications in MPI such as imaging blood flow or tracking medical instruments benefit from sharper reconstructions caused by the adapted total variation regularization. The smooth reconstructions obtained by the commonly applied Tikhonov approach allow a less accurate localization. However, one of the drawbacks of the presented approach might be so called staircaising effects [41] caused by total variation regularization due to the l_1-norm minimization of the gradient. This particularly affects imaging blood flow where the tracer concentration is not necessarily piecewise homogeneous. In contrast, medical instruments are commonly equipped with a marker consisting of tracer with constant concentration such that staircasing is not necessarily an issue. If necessary, staircasing may be avoided by using approaches with higher derivatives, for example, total generalized variation [42].

The present work is the basis for several directions of future research. The promising approach tested in numerical simulations is planned to be validated on real data. Moreover, in the case of complex phantoms with fine structures as in the example of the vascular tree, a combination of directional total variation with an additional sparsity promoting l_1-norm [43] might further improve the reconstruction as it has recently been shown in the context of fused-lasso regularization [29].

The algorithm can be applied to a three-dimensional setup without any adaptation. However, three-dimensional data might require more sophisticated surface detection methods to, for example, improve the three-dimensional reconstruction of vascular trees. It remains future research to incorporate weighting functions suitable for surface detection. New weighting functions may require new algorithmic solutions to minimize the proposed functional.

Acknowledgement

References

[1] B. Gleich and J. Weizenecker. Tomographic imaging using the nonlinear response of magnetic particles. *Nature*, 435 (7046):1214–1217, 2005. doi:10.1038/nature03808.

[2] B. Gleich, J. Weizenecker, and J. Borgert. Experimental results on fast 2D-encoded magnetic particle imaging. *Phys. Med. Biol.*, 53(6):N81–N84, 2008. doi:10.1088/0031-9155/53/6/N01.

[3] J. Weizenecker, B. Gleich, J. Rahmer, H. Dahnke, and J. Borgert. Three-dimensional real-time in vivo magnetic particle imaging. *Phys. Med. Biol.*, 54(5):L1–L10, 2009.

[4] J. Haegele, J. Rahmer, B. Gleich, J. Borgert, H. Wojtczyk, N. Panagiotopoulos, T. M. Buzug, J. Barkhausen, and F. M. Vogt. Magnetic Particle Imaging: Visualization of Instruments for Cardiovascular Intervention. *Radiology*, 265 (3):933–938, 2012.

[5] J. Salamon, M. Hofmann, C. Jung, M. G. Kaul, F. Werner, K. Them, R. Reimer, P. Nielsen, A. vom Scheidt, G. Adam, T. Knopp, and H. Ittrich. Magnetic Particle / Magnetic Resonance Imaging: In-Vitro MPI-Guided Real Time Catheter Tracking and 4D Angioplasty Using a Road Map and Blood Pool Tracer Approach. *PLOS ONE*, 11(6):e0156899, 2016. doi:10.1371/journal.pone.0156899.

[6] T. Knopp, T. F. Sattel, S. Biederer, J. Rahmer, J. Weizenecker, B. Gleich, J. Borgert, and T. M. Buzug. Model-Based Reconstruction for Magnetic Particle Imaging. *IEEE Trans. Med. Imag.*, 29(1):12–18, 2010. doi:10.1109/TMI.2009.2021612.

[7] M. Grüttner, T. Knopp, J. Franke, M. Heidenreich, J. Rahmer, A. Halkola, C. Kaethner, J. Borgert, and T. M. Buzug. On the formulation of the image reconstruction problem in magnetic particle imaging. *Biomed. Tech. / Biomed. Eng.*, 58(6):583–591, 2013. doi:10.1515/bmt-2012-0063.

[8] T. Knopp, S. Biederer, T. F. Sattel, J. Rahmer, J. Weizenecker, B. Gleich, J. Borgert, and T. M. Buzug. 2D model-based reconstruction for magnetic particle imaging. *Med. Phys.*, 37(2):485–491, 2010. doi:10.1118/1.3271258.

[9] T. März and A. Weinmann. Model-Based Reconstruction for Magnetic Particle Imaging in 2D and 3D. arXiv:1605.08095, 2016.

[10] L. R. Croft, P. W. Goodwill, and S. M. Conolly. Relaxation in X-Space Magnetic Particle Imaging. *IEEE Trans. Med. Imag.*, 31(12):2335–2342, 2012. doi:10.1109/TMI.2012.2217979.

[11] J. J. Konkle, P. W. Goodwill, D. W. Hensley, R. D. Orendorff, M. Lustig, and S. M. Conolly. A Convex Formulation for Magnetic Particle Imaging X-Space Reconstruction. *PLOS ONE*, 10(10):e0140137, 2015. doi:10.1371/journal.pone.0140137.

[12] B. Zheng, T. Vazin, P. W. Goodwill, A. Conway, A. Verma, E. U. Saritas, D. Schaffer, and S. M. Conolly. Magnetic Particle Imaging tracks the long-term fate of in vivo neural cell implants with high image contrast. *Sci. Rep.*, 5:14055, 2015. doi:10.1038/srep14055.

[13] P. W. Goodwill and S. M. Conolly. The x-Space Formulation of the Magnetic Particle Imaging process: One-Dimensional Signal, Resolution, Bandwidth, SNR, SAR, and Magnetostimulation. *IEEE Trans. Med. Imag.*, 29(11):1851–1859, 2010. doi:10.1109/TMI.2010.2052284.

[14] P. W. Goodwill and S. M. Conolly. Multidimensional X-Space Magnetic Particle Imaging. *IEEE Trans. Med. Imag.*, 30(9):1581–1590, 2011.

[15] T. Knopp, S. Biederer, T. F. Sattel, and T. M. Buzug. Singular value analysis for Magnetic Particle Imaging. In *IEEE Nuclear Science Symposium*, pages 4525–4529, 2008. doi:10.1109/NSSMIC.2008.4774296.

[16] T. Knopp, J. Rahmer, T. F. Sattel, S. Biederer, J. Weizenecker, B. Gleich, J. Borgert, and T. M. Buzug. Weighted iterative reconstruction for magnetic particle imaging. *Phys. Med. Biol.*, 55(6):1577–1589, 2010. doi:10.1088/0031-9155/55/6/003.

[17] J. Rahmer, J. Weizenecker, B. Gleich, and J. Borgert. Analysis of a 3-D System Function Measured for Magnetic Particle Imaging. *IEEE Trans. Med. Imag.*, 31(6):1289–1299, 2012. doi:10.1109/TMI.2012.2188639.

[18] J. Lampe, C. Bassoy, J. Rahmer, J. Weizenecker, H. Voss, B. Gleich, and J. Borgert. Fast reconstruction in magnetic particle imaging. *Phys Med Biol*, 57(4):1113–1134, 2012. doi:10.1088/0031-9155/57/4/1113.

[19] M. G. Kaul, O. Weber, U. Heinen, A. Reitmeier, T. Mummert, C. Jung, N. Raabe, T. Knopp, H. Ittrich, and G. Adam. Combined Preclinical Magnetic Particle Imaging and Magnetic Resonance Imaging: Initial Results in Mice. *Fortschr. Röntgenstr.*, 187(05):347–352, 2015. doi:10.1055/s-0034-1399344.

[20] T. Knopp and M. Hofmann. Online reconstruction of 3D magnetic particle imaging data. *Phys. Med. Biol.*, 61(11): N257–N267, 2016. doi:10.1088/0031-9155/61/11/N257.

[21] P. Vogel, S. Lother, M.A. Ruckert, W.H. Kullmann, P.M. Jakob, F. Fidler, and V.C. Behr. MRI Meets MPI: A Bimodal MPI-MRI Tomograph. *IEEE Trans. Med. Imag.*, 33(10):1954–1959, 2014. doi:10.1109/TMI.2014.2327515.

[22] J. Franke, U. Heinen, H. Lehr, A. Weber, F. Jaspard, W. Ruhm, M. Heidenreich, and V. Schulz. System Characterization of a Highly Integrated Preclinical Hybrid MPI-MRI Scanner. *IEEE Trans. Med. Imag.*, 35(9):1993–2004, 2016. doi:10.1109/TMI.2016.2542041.

[23] K. Vunckx, A. Atre, K. Baete, A. Reilhac, C. M. Deroose, K. Van Laere, and J. Nuyts. Evaluation of Three MRI-Based Anatomical Priors for Quantitative PET Brain Imaging. *IEEE Trans. Med. Imag.*, 31(3):599–612, 2012. doi:10.1109/TMI.2011.2173766.

[24] M. J. Ehrhardt, K. Thielemans, L. Pizarro, D. Atkinson, S. Ourselin, B. F. Hutton, and S. R. Arridge. Joint reconstruction of PET-MRI by exploiting structural similarity. *Inverse Probl.*, 31(1):015001, 2015. doi:10.1088/0266-5611/31/1/015001.

[25] M. J. Ehrhardt and M. M. Betcke. Multi-Contrast MRI Reconstruction with Structure-Guided Total Variation. *SIAM J. Imaging Sci.*, 9(3):1084–1106, 2016. doi:10.1137/15M1047325.

[26] S. Somayajula, C. Panagiotou, A. Rangarajan, Q. Li, S. R. Arridge, and R. M. Leahy. PET Image Reconstruction Using Information Theoretic Anatomical Priors. *IEEE Trans. Med. Imag.*, 30(3):537–549, 2011. doi:10.1109/TMI.2010.2076827.

[27] Jari P Kaipio, Ville Kolehmainen, Marko Vauhkonen, and Erkki Somersalo. Inverse problems with structural prior information. *Inverse Probl.*, 15(3):713, 1999. doi:10.1088/0266-5611/15/3/306.

[28] D. Kazantsev, S. R. Arridge, S. Pedemonte, A. Bousse, K. Erlandsson, B. F. Hutton, and S. Ourselin. An anatomically driven anisotropic diffusion filtering method for 3D SPECT reconstruction. *Phys. Med. Biol.*, 57(12):3793–3810, 2012. doi:10.1088/0031-9155/57/12/3793.

[29] M. Storath, C. Brandt, M. Hofmann, T. Knopp, J. Salamon, A. Weber, and A. Weinmann. Edge Preserving and Noise Reducing Reconstruction for Magnetic Particle Imaging. *IEEE Trans. Med. Imag.*, 36(1):74–85, 2017. doi:10.1109/TMI.2016.2593954.

[30] L. I. Rudin, S. Osher, and E. Fatemi. Nonlinear total variation based noise removal algorithms. *Physica D*, 60(1): 259–268, 1992. doi:10.1016/0167-2789(92)90242-F.

[31] X. Bresson, S. Esedoglu, P. Vandergheynst, J.-P. Thiran, and S. Osher. Fast Global Minimization of the Active

Contour/Snake Model. *J. Math. Imaging Vis.*, 28(2):151–167, 2007. doi:10.1007/s10851-007-0002-0.

[32] M. Unger, T. Pock, W. Trobin, D. Cremers, and H. Bischof. TVSeg-Interactive Total Variation Based Image Segmentation. In *BMVC*, pages 40.1–40.10, 2008. doi:10.5244/C.22.40.

[33] I. Bayram and M. E. Kamasak. Directional Total Variation. *IEEE Signal Process. Lett.*, 19(12):781–784, 2012. doi:10.1109/LSP.2012.2220349.

[34] S. Boyd. Distributed Optimization and Statistical Learning via the Alternating Direction Method of Multipliers. *Foundations and Trends® in Machine Learning*, 3(1):1–122, 2011. doi:10.1561/2200000016.

[35] R. Barrett, M. Berry, T. F. Chan, J. Demmel, J. M. Donato, J. Dongarra, V. Eijkhout, R. Pozo, C. Romine, and H. Van der Vorst. *Templates for the Solution of Linear Systems: Building Blocks for Iterative Methods*. SIAM, Philadelphia, PA, 1994.

[36] A. Chambolle. An Algorithm for Total Variation Minimization and Applications. *J. Math. Imaging Vision*, 20(1):89–97, 2004. doi:10.1023/B:JMIV.0000011325.36760.1e.

[37] A. Beck and M. Teboulle. A Fast Iterative Shrinkage-Thresholding Algorithm for Linear Inverse Problems. *SIAM J. Imaging Sci.*, 2(1):183–202, 2009. doi:10.1137/080716542.

[38] J. Weizenecker, B. Gleich, and J. Borgert. A simulation study on the resolution and sensitivity of magnetic particle imaging. *Phys. Med. Biol.*, 52(21):6363–6374, 2007. doi:10.1088/0031-9155/52/21/001.

[39] P. C. Hansen. REGULARIZATION TOOLS: A Matlab package for analysis and solution of discrete ill-posed problems. *Numer. Algorithms*, 6(1):1–35, 1994. doi:10.1007/BF02149761.

[40] T. Knopp, T. Viereck, G. Bringout, M. Ahlborg, J. Rahmer, and M. Hofmann. MDF: Magnetic Particle Imaging Data Format. *arXiv:1602.06072 [physics.med-ph]*, 2016.

[41] T. Chan, S. Esedoglu, F. Park, and A. Yip. Recent developments in total variation image restoration. In *Mathematical Models of Computer Vision*, 2005.

[42] F. Knoll, K. Bredies, T. Pock, and R. Stollberger. Second order total generalized variation (TGV) for MRI. *Magn. Reson. Med.*, 65(2):480–491, 2011. doi:10.1002/mrm.22595.

[43] B. Jin and P. Maass. Sparsity regularization for parameter identification problems. *Inverse Probl.*, 28(12):123001, 2012. doi:10.1088/0266-5611/28/12/123001.